Diagnostics for the Tropics: Some (Cautious) Uses of Satellite Data

Duane Waliser[1], Jui-Lin (Frank) Li[1], Baijun Tian[1], Xianan Jiang[2]

[1]Jet Propulsion Laboratory, California Institute of Technology, Pasadena, CA
[2]Joint Institute for Regional Earth System Science & Engineering
University of California, Los Angeles, California

1. Introduction

The accurate representation and forecasting of tropical atmospheric variability has been challenging, notably because of the prevalence of sub-grid scale clouds and convection at the typical resolutions of operational forecast models and because the balance of the momentum, mass and heat equations is more tenuous across the many terms that play a role in these conservation laws. Another difficulty is that the range of important space scales extends up to global and down to the cloud microphysical scale, and in many cases the phenomena and processes are just poorly understood. In addition, we face a significant lack of understanding of how mesoscale, synoptic-scale and planetary-scale phenomena interact as a coupled dynamical system. This lack of fundamental knowledge and practical capability leaves us disadvantaged in modeling and predicting prominent phenomena of the tropical atmosphere such as the ITCZ, ENSO, TBO, monsoons and their active/break periods, the MJO, subtropical stratus decks, easterly waves, tropical cyclones, bulk budgets of cloud microphysical quantities, and even the diurnal cycle (the most basic forced variability of atmospheric motion). Unfortunately, a poor model representation of the tropics isn't limited to the Tropics, but rather the shortcomings extend into the representation of the extra-tropics via tropical-extratropical interactions, such as through poleward migration of synoptic systems or through initiating Rossby wave trains that can involve a range of processes and time scales (e.g., synoptic, MJO/intraseasonal, ENSO/seasonal-to-interannual). Figure 1 provides a cross-section of phenomena that illustrate well-known shortcomings in our model representations of the Tropics, including mean climate, variability, climate change projections and extra-tropical weather forecasts.

Achieving better model representation of the Tropics will require judicious ways of utilizing observations, particularly in the form of developing diagnostics and metrics that can probe and characterize processes and structure. Fortunately, there are a host of new satellite measurements that offer altogether new opportunities in this regard. This presentation describes a few of these and illustrates in some cases their comparison to model simulation and forecast output. These include an emphasis on vertical structure, with opportunities recently arising from temperature and moisture profiles from the Atmospheric Infrared Sounder (AIRS), the TRMM retrievals of latent heating structure, and cloud vertical structure from CloudSat. While the opportunities these new data are welcome, they come with a need to be cautious in the application of the data in a model evaluation context as there are issues that need to be considered in regards to model-data equivalence, sampling, etc Emphasis in this discussion is also placed on the needs and successes of programmatic activities

(e.g., US CLIVAR MJO Working Group) that have developed formal diagnostics that can be utilized by the community in a more consistent and quantitative fashion. The presentation concludes with suggestions of future work and directions.

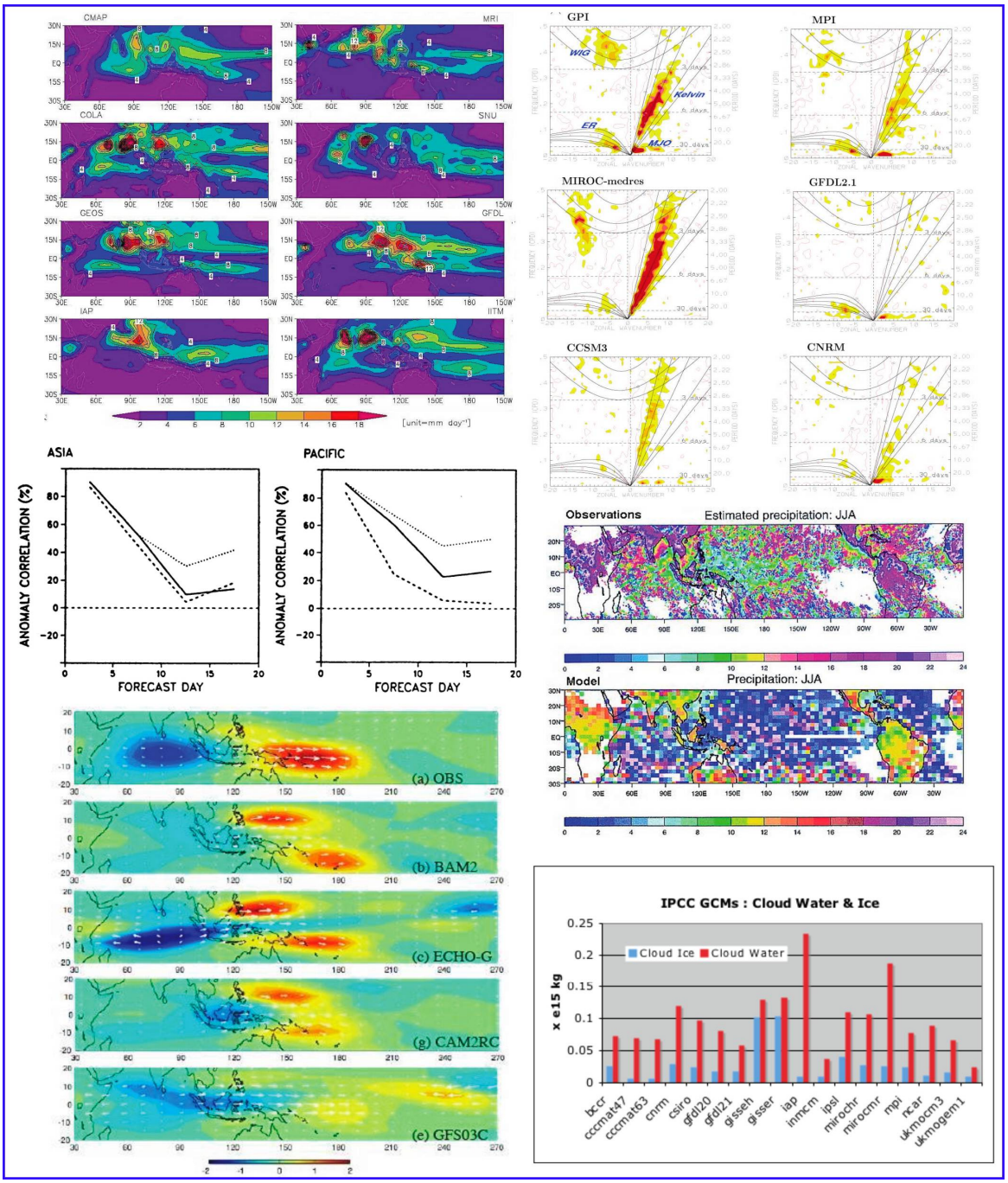

Figure 1. [Clockwise] (upper left) Climatological JJA precipitation from observations (upper left) and a select number of GCMs (8). (upper right) Wavenumber-frequency diagrams of equatorial precipitation from observations (upper left) and a select number of GCMs (9). (middle right) Phase of the diurnal cycle in precipitation for JJA from observations (upper) and a GCM (lower) (10). (lower right) Total tropical (30N-30S) integrated cloud water and ice from the 20th century simulations contributed to the 4th IPCC assessment. (lower left) Zero-lag regression of band-pass/MJO filtered U850 (vectors) and precipitation (colors, mm day-1) upon filtered U850 at 160°E and 0°N (11). (middle left) Extra-tropical 200 hPa potential vorticity forecast skill versus lead-time for operational.

2. Results

2.1. More Traditional Diagnostics of the MJO

The Madden-Julian Oscillation (MJO) (Madden and Julian 1971, 1972) interacts with, and influences, a wide range of weather and climate phenomena (e.g., monsoons, ENSO, tropical storms, mid-latitude weather), and represents an important, and as yet unexploited, source of predictability at the subseasonal time scale (Lau and Waliser 2005; Zhang 2005). Despite the important role of the MJO in our climate and weather systems, current global circulation models (GCMs) exhibit considerable shortcomings in representing this phenomenon. These shortcomings have been documented in a number of multi-model comparison studies over the last decade (e.g., Slingo et al. 2005; Lin et al. 2006; Zhang et al. 2006). However, diagnosis of model performance has been challenging, and model progress has been difficult to track, due to the lack of a coherent and standardized set of MJO diagnostics. One of the chief objectives of the US CLIVAR MJO Working Group (2006-2009; http://www.usclivar.org/mjo.php; hereafter MJOWG) was the development of observation-based diagnostics for objectively evaluating global model simulations of the MJO in a consistent framework. A sample of the diagnostics developed from this activity is presented and in some cases shown in the context of a multi-model comparison. For the full range of diagnostics developed, along with the details regarding the intent and justification for the diagnostics, more precise specifications for their calculation, and more complete illustrations of their application, the reader is referred to CLIVAR MJO Working Group (2009) and Kim et al. (2010), as well as the above listed website which has a link to the graphics, code, calculation specifications, and discussion of the diagnostics.

Figure 2 illustrates a few of the diagnostics developed by the MJOWG and some of the important characteristics of the framework. For example, there are three types of diagnostics, simple (Level 1), more advanced (Level 2) and diagnostics concerning the mean state and other aspects. Level 1 diagnostics are meant to provide a basic indication of model spatial and temporal intraseasonal variability that can be easily understood and calculated by the non-MJO expert. Ease of use dictated that the analytic procedures be as simple and uniform as possible for summer and winter calculations. In particular, Level 1 diagnostics include an assessment of intraseasonal and total variance (e.g., Fig. 3), time series spectral analysis over key spatial domains (e.g., upper left Figure 2) and univariate empirical orthogonal function (EOF) analysis of bandpass filtered data (not shown). Lag-correlation analysis of bandpass filtered wind and convective variables is also used to assess both eastward equatorial propagation during both boreal summer and winter, and northward propagation in the eastern Hemisphere during boreal summer (not shown). Variables used in Level 1 diagnostics include OLR, precipitation and zonal wind at 850 and 200 hPa.

Level 2 diagnostics provide a more comprehensive diagnosis of the MJO through multivariate EOF analysis and wavenumber-frequency decomposition (e.g., lower left of Figure 2). The multivariate EOF analysis is based on OLR and zonal wind at 850 and 200 hPa [*Wheeler and Hendon*, 2004]. The dominant intraseasonal PCs from multivariate EOF analysis are used to generate MJO lifecycle composites (e.g., upper right Figure 2), and coherence-squared and phase between the PC's are calculated to determine the fidelity of the eastward propagation (not shown). However, a number of other variables are included in life cycle composites. Multi-scale interactions are also assessed using cross-spectral analysis (coherence squared and phase) between variables (not shown).

In addition to the Level 1 and Level 2 diagnostics, supplementary diagnostics are developed for a number of relevant mean state variables (e.g., lower right of Figure 2). As described in past studies [e.g., *Slingo et al.*, 1996; *Hendon*, 2000; *Inness et al.*, 2003; *Waliser et al.*, 2003a; *Sperber et al.*, 2005; *Zhang et al.*, 2006b], the ability of a model to simulate the MJO is intimately related to its ability to simulate the mean climate, especially associated with the spatial distribution of mean convection and surface westerly winds that tend to occur over the warmest SST. Finally, the occurrence of the MJO is highly episodic [e.g., *Salby and Hendon*, 1994] with the relationship to interannual variation in SST being rather complex, albeit weak [e.g., *Slingo et al.*, 1996; *Hendon et al.*, 1999; *Kessler*, 2001; *Lau*, 2005; *Hendon et al.*, 2007]. Efforts at simulating the character of this relationship have had mixed success [e.g., *Slingo et al.*, 1996; *Gualdi et al.*, 1999b; *Waliser et al.*, 2001], and thus an analysis of interannual variability of MJO activity is also included as a supplementary diagnostic (not shown).

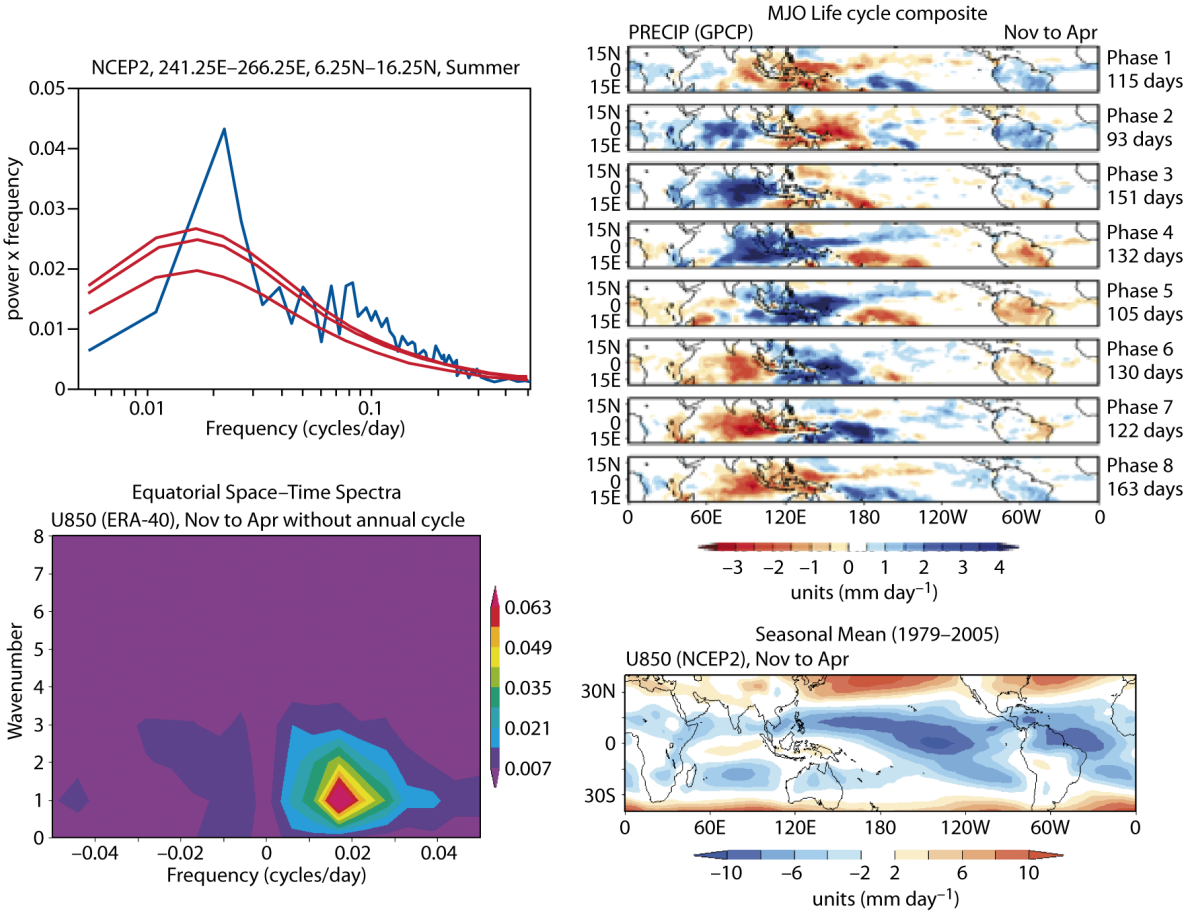

Figure 2. (upper left) May-Oct power spectra of 850 hPa zonal wind over the eastern tropical Pacific from NCEP/NCAR. (lower left) Nov-Apr wavenumber-frequency spectra of 10°N-10°S averaged for 850 hPa zonal wind for ERA-40). (upper right) Composite Nov-Apr 20-100 day CMAP precipitation anomalies (vectors) as a function of MJO phase. (lower right) Nov-Apr NCEP/NCAR 850 hPa multi-year (1979-2005) mean zonal wind. For further details, see CLIVAR MJO Working Group (2009).

2.2. Application of MJO Diagnostics to Multi-Model Evaluation

In this section, a subset of the MJOWG diagnostics is used in the context of a GCM evaluation relative to their MJO representation (Kim et al. 2010). Specifically, eight climate models are examined with a focus on their boreal winter (Nov-Apr) behavior. The models include three coupled and five uncoupled GCM simulations, each providing roughly 20 years of daily output for the evaluation. The models have various horizontal (from 2.8 to 1 degree) and vertical (from 19 to 72 levels) resolutions in their atmospheric components. Seven of the models are conventional GCMs in which convection and clouds are parameterized, while one model, superparameterized CAM (SPCAM), utilizes embedded 2-dimensional cloud resolving models for these processes (Khairoutdinov et al. 2005). Further details regarding the models and their relevant physical parameterizations can be found in Kim et al. (2010).

To see how the magnitude and geographical distribution of intraseasonal variability are simulated, Figure 3 shows maps of the 20-100 day filtered variance of U850 and precipitation. In observations (Fig. 3a), the U850 and precipitation variance maxima are located in eastern Indian Ocean, western Pacific and south of Maritime Continent region. The intraseasonal variability of both U850 and precipitation is weak over the Maritime Continent. These attributes are most realistically represented in CAM3z, ECHAM4/OPYC, SNU, and SPCAM (Figs. 3c, 3f, 3h, and 3i). Based on the pattern correlations (see Kim et al.), CAM3z and SPCAM (Figs. 3c and 3i) demonstrate an improved intraseasonal variance pattern compared to the current standard version of the model, CAM3.5 (Fig. 3b), although they have variance much higher than observed. Earlier versions of the CAM model also exhibited difficulty in simulating intraseasonal variations (Sperber 2004) and other modifications of the convection scheme in CAM have led to improved intraseasonal behavior (Maloney and Hartmann 2001; Liu et al. 2005; Zhang and Mu 2005a). Both the GEOS-5 and CAM3.5 have weaker than observed precipitation variance.

In Fig. 4 equatorial wavenumber-frequency plots (Hayashi 1979) of precipitation and U850 are illustrated to isolate the characteristic spatial and temporal scales on which variability is organized. Consistent with the results of previous studies (Weickmann et al. 1985; Kiladis and Weickmann 1992; Zhang et al. 2006), the dominant spatial scale of precipitation in observations is zonal wavenumbers 1 to 3 and for U850 it is zonal wavenumber 1 for periods of 30-80 days (Fig. 4a). These scales distinguish the MJO from other convectively coupled equatorial waves (Wheeler and Kiladis 1999). For U850, ECHAM4/OPYC produces a spectrum similar to observation (Fig. 4f), whereas CFS and SPCAM overestimate the power for periods of 30 to 80 days (Figs. 4d and 4i). For CAM3.5 and CM2.1, the eastward propagating power tends to be concentrated at low-frequencies (period > 80 days; Figs. 4b and 4e). Most models (CAM3.5, CFS, CM2.1, ECHAM4/OPYC, GEOS5, and SNU) are less successful at representing the 30-80 spectral peak for precipitation than that of U850. Consistent with Zhang et al. (2006), these results suggest a lack of coherence between the simulation of intraseasonal precipitation and U850.

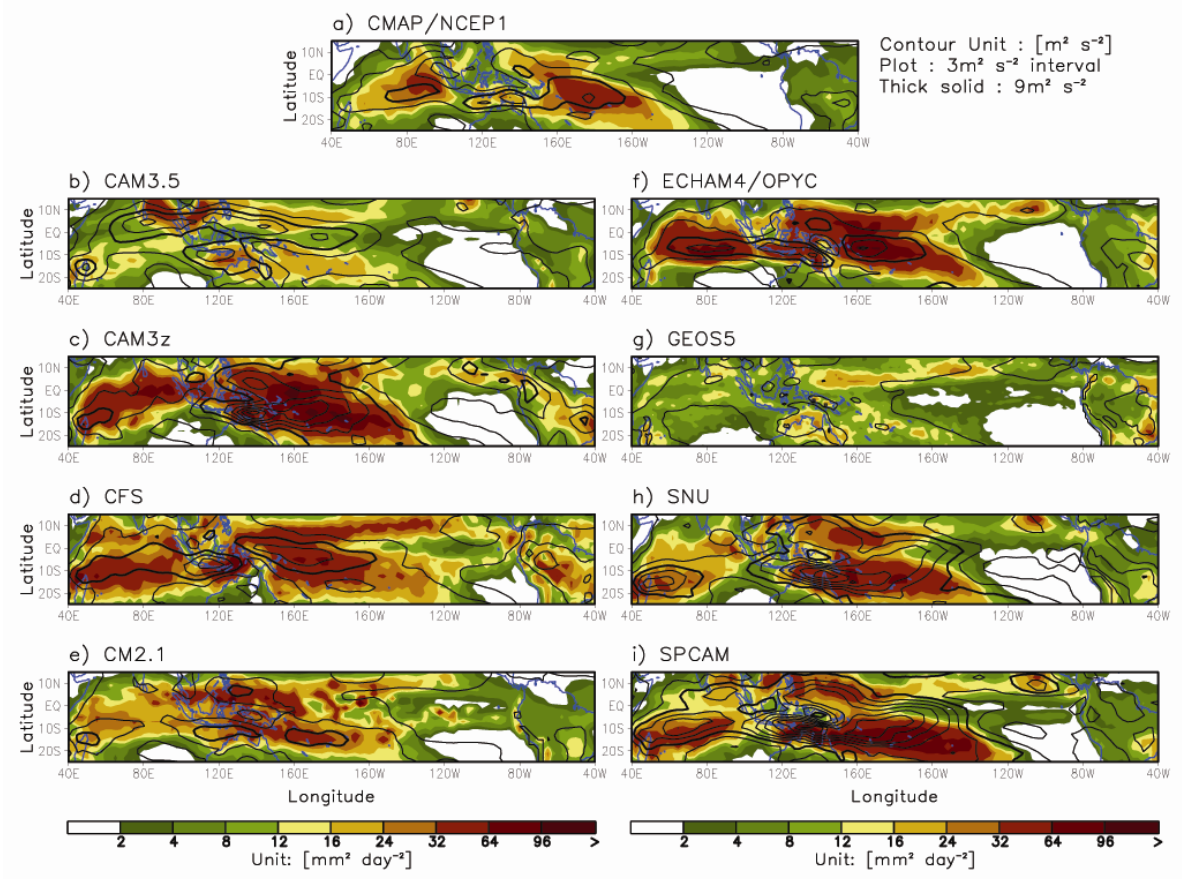

Figure 3. Variance of 20-100 day band pass filtered precipitation and 850hPa zonal wind. Contours of 850hPa zonal wind variance are plotted every 3 m^2 s^{-2}, with the 9 m^2 s^{-2} line represented by the thick solid line. The unit is mm^2 day^{-2} for precipitation and m^2 s^{-2} for zonal wind. Kim et al. (2010).

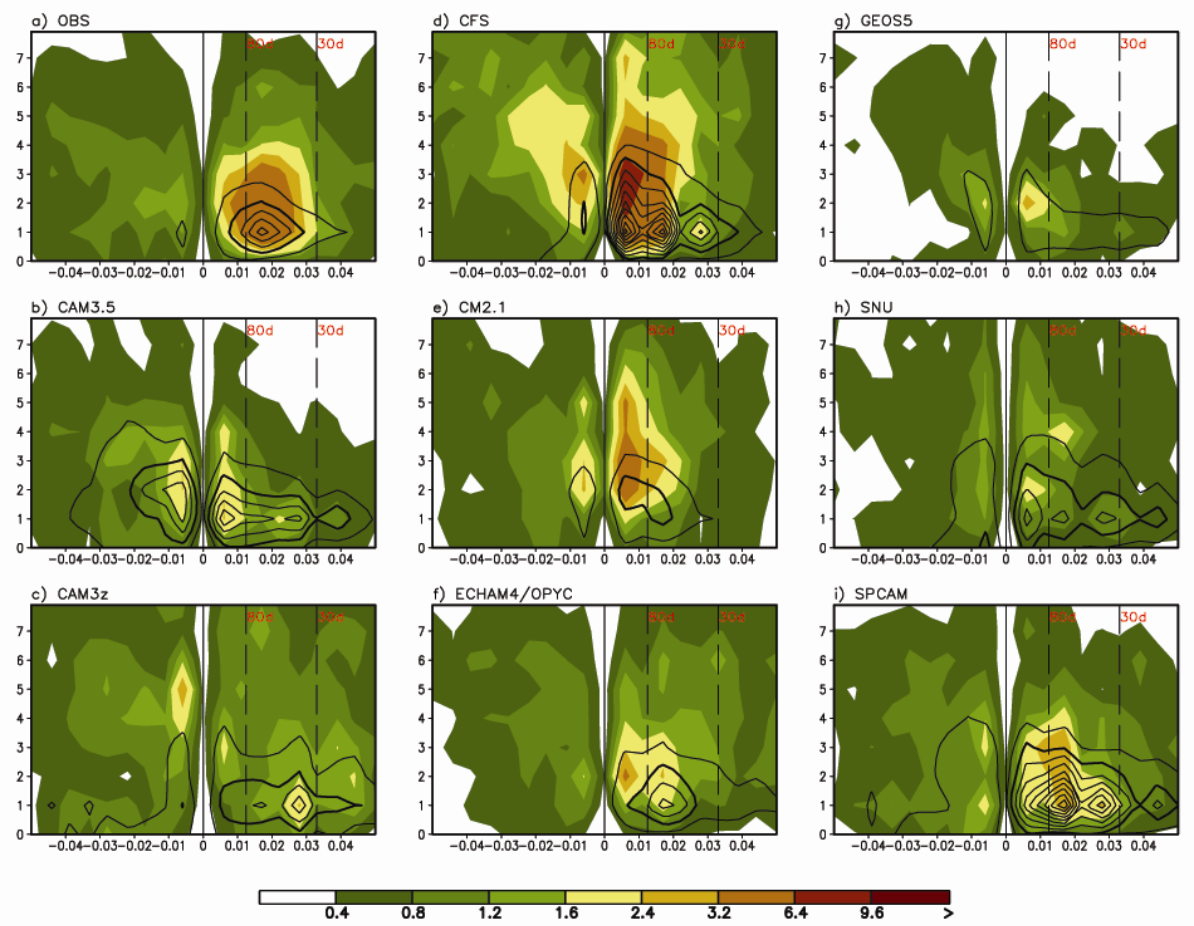

Figure 4. November-April wavenumber-frequency spectra of 10°N-10°S averaged precipitation (shaded) and 850hPa zonal wind (contoured). a) CMAP/NCEP/NCAR, b) CAM3.5, c) CAM3z, d) CFS, e) CM2.1, f) ECHAM4/OPYC, g) GEOS5, h) SNU, and i) SPCAM. Individual November-April spectra were calculated for each year, and then averaged over all years of data. Only the climatological seasonal cycle and time mean for each November-April segment were removed before calculation of the spectra. Units for the precipitation (zonal wind) spectrum are $mm^2\ day^{-2}$ ($m^2\ s^{-2}$) per frequency interval per wavenumber interval. The bandwidth is $(180\ d)^{-1}$. Kim et al. (2010).

MJO life cycle composites are constructed by averaging band pass filtered anomalies across all days that fall within a given phase when the MJO amplitude is greater or equal to 1. The upper right panel of Figure 2 shows composite maps of precipitation over the MJO lifecycle. Figure 5 shows a different presentation of lifecycle in terms of phase-longitude diagrams of OLR and surface latent heat flux anomalies. Observations show two convective maxima (Fig. 5a), one over the eastern Indian Ocean and the other over the west Pacific Ocean with weakened convection over the Maritime Continent. The strong convective signal is preceded by a negative evaporation anomaly while positive evaporation anomalies follow the enhanced convection. Models generally capture this relationship although the amplitude of the evaporation anomaly associated with convection is especially weak in CAM3.5 and GEOS5 (Figs. 5b and 5g) in which the convective anomalies exhibit little or no eastward propagation. Contrary to observations, the CFS model (Fig. 5d) has its largest latent heat flux signal over the eastern Pacific Ocean, and largest OLR amplitude in the Atlantic.

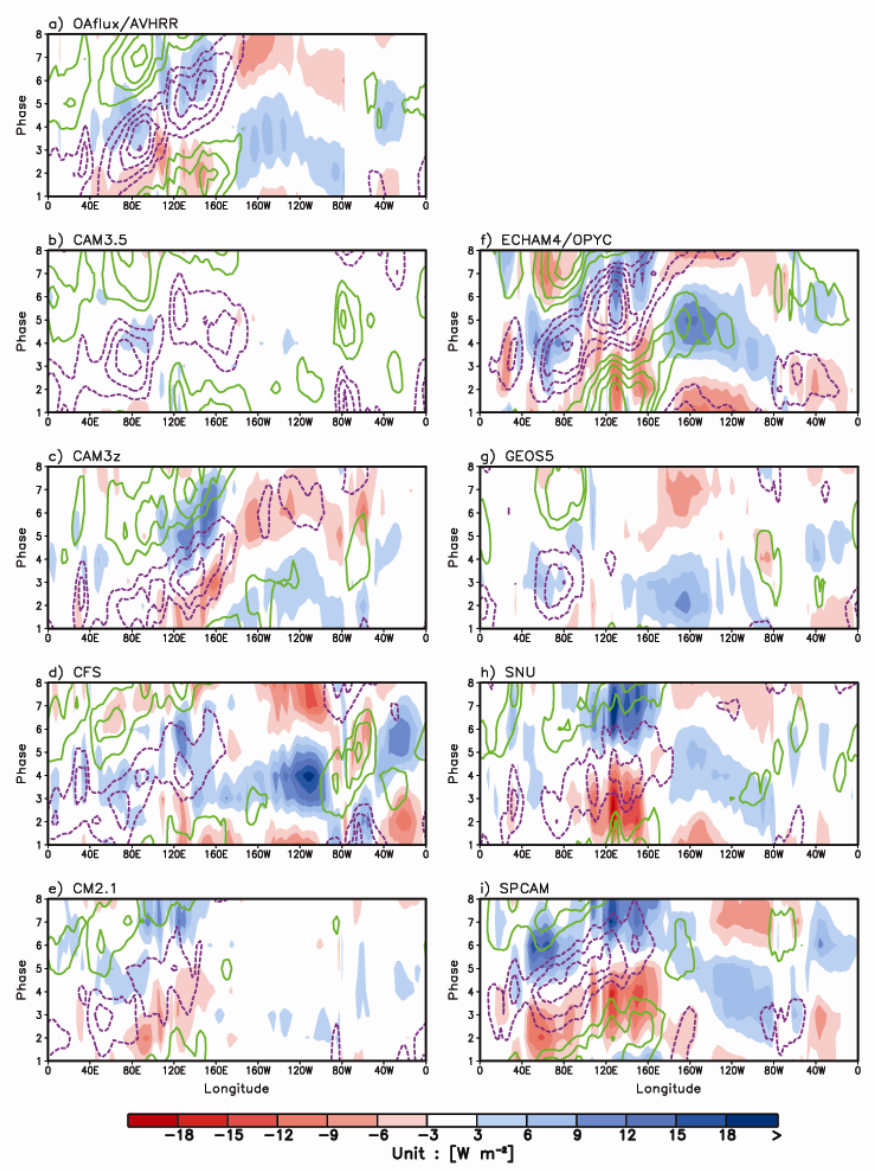

Figure 5. Phase-longitude diagram of OLR (contour, plotted every 5 Wm^{-2}, green-positive/purple-negative) and surface latent heat flux (Wm^{-2}; shaded). Phases are from MJO life-cycle composite and values are 5°S-5°N averaged. Kim et al. (2010).

2.3. Exploring the Use of Newer Satellite Observations

2.3.1. AIRS Temperature and Water Vapor and the MJO

The Atmospheric Infrared Sounder (AIRS)/Advanced Microwave Sounding Unit (AMSU) (Chahine et al. 2006) on the NASA Aqua mission provides a new opportunity to document the large-scale three-dimensional moist thermodynamic structure and spatial-temporal evolution of the MJO (e.g., Tian et al. 2006; Fu et al. 2006; Yang et al. 2008). This analysis builds on that of Tian et al. (2006) who performed such an analysis using the first 2.5-years (2002-2005) of AIRS. Here, we further illustrate this potential model diagnostic using the currently available 7-year AIRS data (2002-2009). Moreover, to examine the sensitivity of the diagnostics and illustrate the sorts of issues that arise in constructing diagnostics of this sort, we test its dependence on AIRS data record (2.5 versus 7 years), the MJO analysis method employed. We also compare the AIRS result with the ECMWF Interim reanalysis (ERA-Int) to evaluate the performance of ERA-Int, the new global reanalysis data set from ECMWF, in describing the large-scale vertical moist thermodynamic structure of the MJO.

Two MJO analysis methods (e.g., MJO index definitions and compositing procedures) were employed for this study. Method 1 is the MJO analysis method used by Waliser et al. (2003) and Tian et al. (2006). Briefly, all data were first binned into pentad (5-day) values and then intraseasonal anomalies of the pentad data were obtained by removing the climatological seasonal cycle and filtering via a 30–90-day band pass filter. To isolate the dominant structure of the MJO, an extended empirical orthogonal function (EEOF) analysis using time lags of ±5 pentads (i.e. 11 pentads total) was applied on boreal winter (November–April) intraseasonal filtered rainfall anomaly from 1998 to 2009 for the tropical Indian Ocean and western Pacific (30°S-30°N, 30°E-150°W). The spatial–temporal pattern for the first EEOF mode, shown in Figure 6a, is very similar to that in Tian et al. (2006) (their Figure 1) except for a pentad phase shift which depicts the typical eastward propagation of MJO convective activity. Next, MJO events were chosen based on maxima in the pentad principal component (PC) time series of the first EEOF mode if their amplitudes are greater than +1 standard deviation. Figure 6b shows the selected 18 MJO events as indicated by crosses for the boreal winter from 2002 to 2009. For each selected MJO event, the corresponding 11-pentad anomalies were extracted. A composite MJO cycle (11 pentads) was then obtained by averaging the selected MJO events.

Method 2 is the MJO analysis method introduced by Wheeler and Hendon (2004) and has been adopted widely by the MJO community (e.g., Waliser et al. 2009). Briefly, the intraseasonal anomalies of daily data were obtained by removing the climatological seasonal cycle and filtering via a 30–90-day band pass filter. Then, a composite MJO cycle (8 phases) was calculated by averaging daily anomalies for each phase of the MJO cycle. The MJO phase for each day is determined by the Real-time Multivariate MJO (RMM) index available from 1974 to present at http://www.cawcr.gov.au/bmrc/clfor/cfstaff/matw/maproom/RMM/. The RMM index is a pair of PC time series, called RMM1 and RMM2, and is the projection of the daily observed NOAA outgoing longwave radiation (OLR) and NCEP/NCAR reanalysis and/or GASP analysis 850- and 200-hPa zonal winds, with the annual cycle and components of interannual variability removed, on a pair of multiple-variable empirical orthogonal functions (EOFs). Such two EOFs are the leading and second EOFs of the combined daily intraseasonal filtered fields of near-equatorially averaged (15°S-15°N) NOAA OLR and NCEP/NCAR 850- and 200-hPa zonal winds for all seasons from 1979 to 2001 (23 years). These two EOFs describe the key features of the MJO, such as the eastward propagation of convection anomalies in the Eastern Hemisphere, the out-of-phase relationship between lower and

upper-tropospheric wind anomalies, and the predominance of lower-tropospheric westerly anomalies near and to the west of enhanced convection. Figure 6c shows the (RMM1, RMM2) phase space for all days in boreal winter from 2002 to 2009 and the number of days for each phase of the composite MJO cycle. Only days with strong MJO activity ($RMM1^2+RMM1^2>=1$) are considered.

Figure 7 shows the composite MJO cycle of equatorial mean (8°S-8°N) pressure-longitude cross sections of specific humidity anomalies (gm/kg) in color shading based on (a) the 7-year pentad AIRS data and the MJO analysis Method 1, (b) the 7-year daily AIRS data and the MJO analysis Method 2, (c) the 7-year daily ERA-Int data and the MJO analysis Method 2. The overlaid solid black lines denote TRMM rainfall anomalies (mm day^{-1}, scales at right) for the same period as the AIRS and ERA-Int data. Figure 8 presents a similar MJO cycle as in Figure 7 but for temperature. For Figures 7a and 8a that are based on the 7-year pentad AIRS data and the MJO analysis Method 1, the lags from -2 to +5 pentads of the MJO cycle are shown, which is roughly corresponding to the phases 1 to 8 of the MJO cycle shown in Figures 7b, 7c, 8b, and 8c that are based on the 7-year daily AIRS/ERA-Int data and the MJO analysis Method 2. Furthermore, the lags from -2 to +2 pentads of the MJO cycle shown in the Figures 7a and 8a are roughly corresponding to the lags from -1 to +3 pentads of the MJO cycle in the Figures 3 and 7 of Tian et al. (2006) that are both based on the pentad AIRS data and the MJO analysis Method 1 but with different data record (2.5 versus 7 years).

First, the comparison of the current Figures 7a and 8a to the Figures 3 and 7 in Tian et al. (2006) indicates the large-scale vertical moist thermodynamic structures of the MJO are consistent with each other between the 2.5- and 7-year AIRS data records. This demonstrates that for this particular field and phenomena, a few years of events captures the main elements of the signal. For example, both studies (Tian et al, (2006) and this analysis) show specific humidity anomalies of around ± 0.5 gm/kg with different vertical structures as a function of longitude and convection anomaly. Over the equatorial Indian Ocean and western Pacific, where MJO convection anomaly is large, the specific humidity anomalies (~0.4 gm kg^{-1}) exhibit a westward tilt structure with height and propagate eastward along the eastward propagation of convection anomaly. During the convectively active phase of the MJO cycle (strong enhanced convection), moist anomalies are generally found throughout the free troposphere (above 850 hPa) with maxima in the middle and lower troposphere. Vice versa for the convectively inactive phase of the MJO cycle (strong suppressed convection). However, during the transition or developing phase of the MJO cycle (weak convection anomaly between inactive and active phases) (e.g., Kikuchi and Takayabu 2004; Agudelo et al. 2006), specific humidity anomalies show a bimodal vertical structure with strong moist or dry anomalies in the lower troposphere (below 500 hPa) and weak specific humidity anomalies above with the opposite sign. As a result, enhanced convection is generally preceded by lower-tropospheric (below 500 hPa) moist anomalies and followed by lower-tropospheric dry anomalies, both in time (~10 days) and space (~30° longitude). Over the equatorial central and eastern Pacific, where MJO convection anomaly is small, specific humidity anomalies are surprisingly large (~0.4 gm kg^{-1}) and mainly confined in the lower troposphere (below 500 hPa) with possible small anomalies with an opposite sign above. This is especially evident over the equatorial eastern Pacific along the coat of South America. Furthermore, the specific humidity anomalies exhibit an eastward tilt structure with height over the equatorial central Pacific. Similar agreement and general propagation characteristics are also found for the temperature field and won't be elaborated on here (see Tian et al. 2006).

Second, the comparison of Figures 7a and 8a to Figures 7b and 8b indicates a strong consistency in the large-scale vertical moist thermodynamic structure of the MJO except for minor differences in magnitude using different temporal resolutions (pentad versus daily) and MJO analysis methods (Method 1 versus 2). This demonstrates that the large-scale vertical moist thermodynamic structure of the MJO, as indicated by this diagnostic, is also independent of the AIRS data temporal resolution and MJO analysis method employed. As a final illustration, comparison of Figures 7b and 8b to Figures 7c and 8c indicates a general good agreement in the large-scale vertical moist thermodynamic structure of the MJO between AIRS and ERA-Int. However, the AIRS results seem to be drier in moist regions and moister in dry regions compared to ECMWF results. Nevertheless, the ERA-Int data seem doing very well in depicting the large-scale moist thermodynamic structure of the MJO in comparison to AIRS observations, at least relative to NCEP/NCAR which examined previously in Tian et al. (2006).

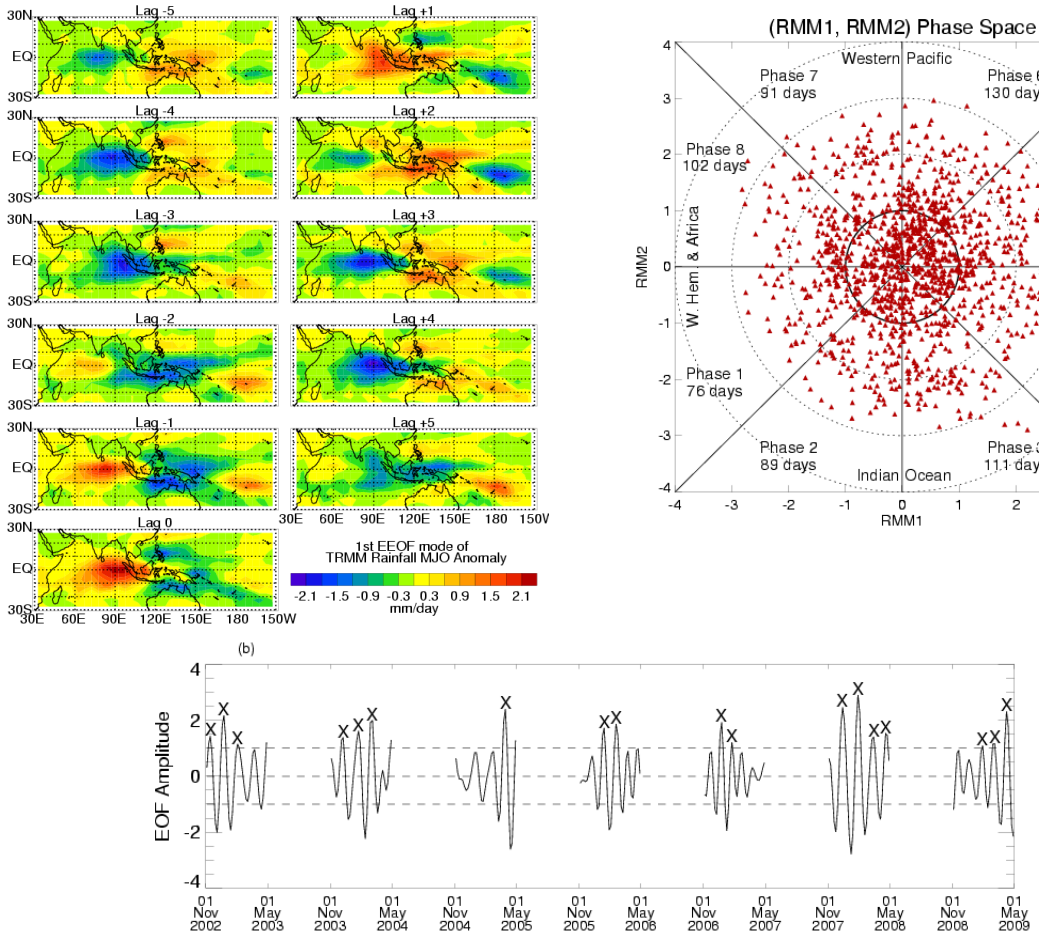

Figure 6: (a) Spatial–temporal pattern of the first EEOF mode of boreal winter (November–April) TRMM rainfall MJO anomaly over the tropical Indian Ocean and western Pacific (30°S–30°N, 30°E–150°W). (b) Principal component (PC) time series based on the first EEOF mode in panel a for the AIRS data period (2002-2009). The crosses indicate the dates of 18 selected MJO events based on maxima in the PC time series. The dashed lines show the PC amplitude of ±1 and 0. The unit for the lag is pentad. (c) (RMM1, RMM2) phase space for all days in boreal winter from 2002 to 2009 and the number of days for each phase of the MJO cycle. Eight defined phases of the phase space are labeled to indicate the eastward propagation of the MJO in one MJO cycle. Also labeled are the approximate locations of the enhanced convective signal of the MJO for that location of the phase space, e.g., the ''Indian Ocean'' for phases 2 and 3.

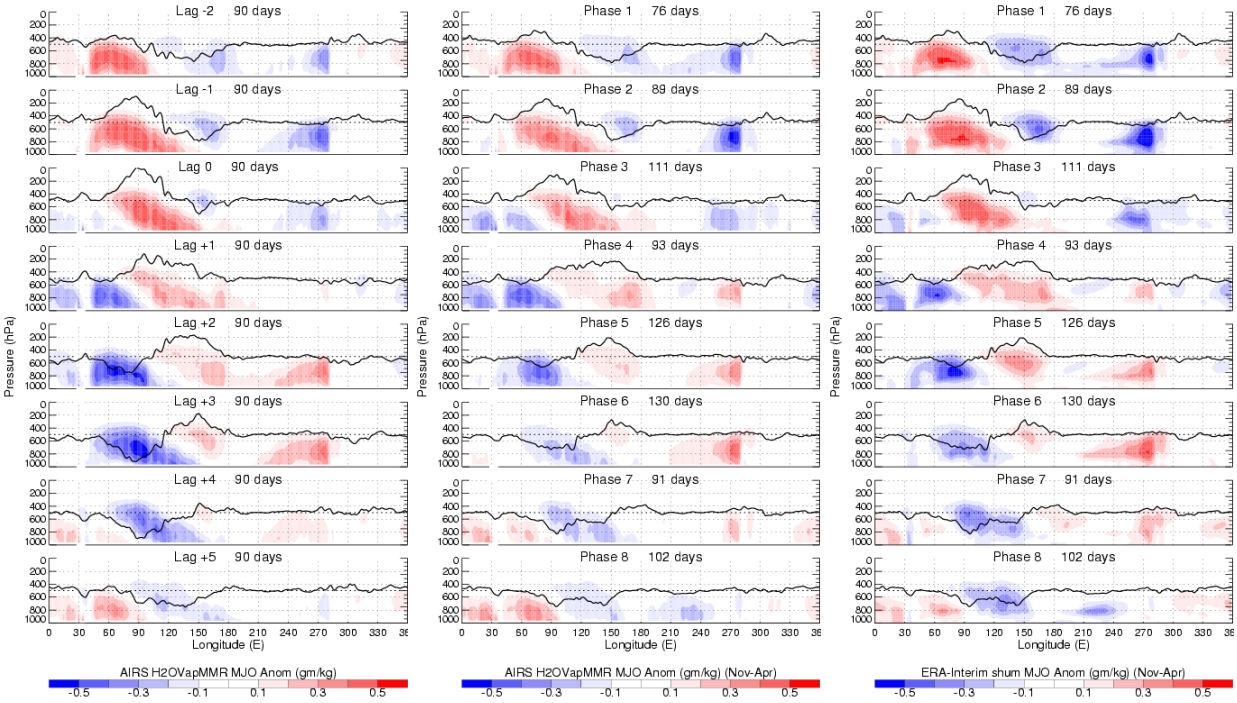

Figure 7: Composite MJO cycle of equatorial mean (8°S-8°N) pressure-longitude cross sections of specific humidity anomalies (gm/kg) in color shading based on (a) the 7-year pentad AIRS data and the MJO analysis Method 1, (b) the 7-year daily AIRS data and the MJO analysis Method 2, (c) the7-year daily ERA-Int data and the MJO analysis Method 2. The overlaid solid black lines denote TRMM rainfall anomalies (mm day^{-1}, scales at right) for the same period for the AIRS and ERA-Int data.

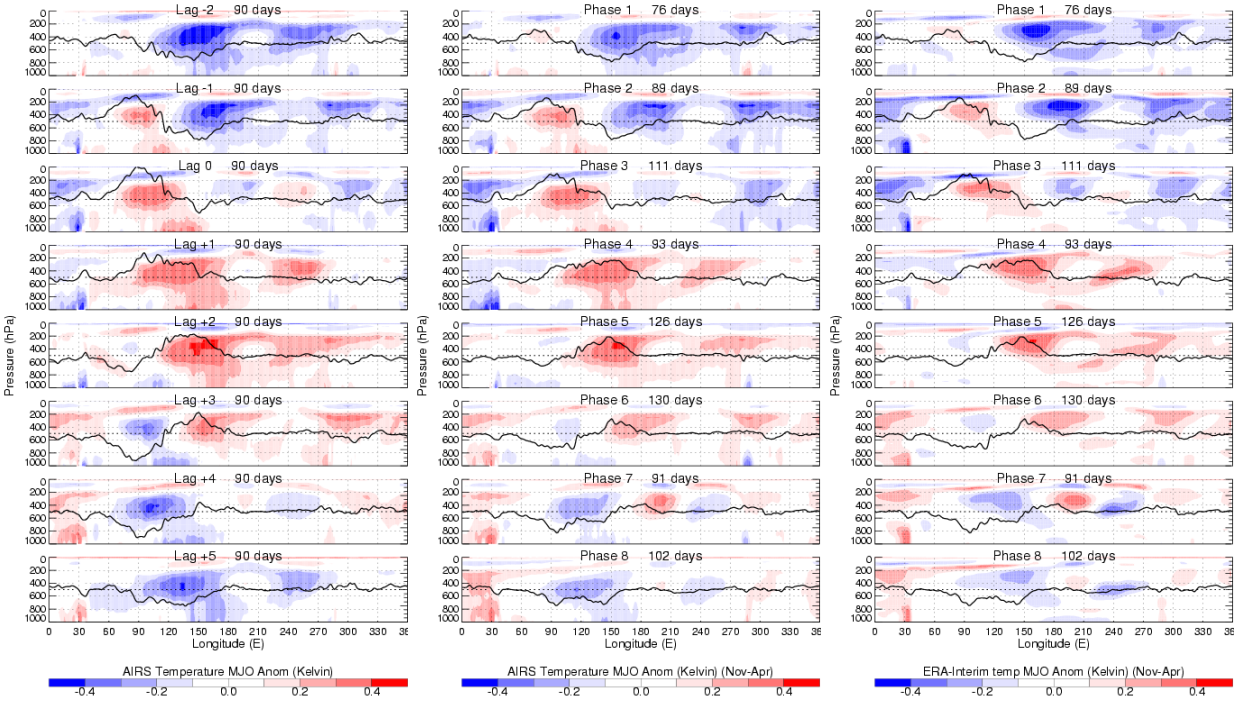

Figure 8: As in Figure 7, except for temperature (K).

In summary, the large-scale vertical moist thermodynamic structure of the MJO from our earlier study (Tian et al. 2006) that are based on the first 2.5-year (2002-2005) pentad AIRS data and the MJO analysis Method 1 was further examined here using the current available 7-year AIRS data (2002-2009) to test the dependence of our results (Tian et al. 2006) on different AIRS data records (2.5 versus 7 years), different AIRS data temporal resolutions (daily versus pentad), and different MJO analysis methods (Method 1 versus 2). The current analysis indicates that our earlier results (Tian et al. 2006) are robust and independent of the AIRS data record, AIRS data temporal resolution and MJO analysis method employed. Furthermore, the large-scale vertical moist thermodynamic structures of the MJO from AIRS and ERA-Int data are also compared to evaluate the performance of ERA-Int in describing the large-scale vertical moist thermodynamic structure of the MJO. Our results indicate that the ERA-Int seems doing very well in this regard although AIRS results seem to be drier in moist regions and moister in dry regions compared to ERA-Int results. These results will provide a useful metric for climate model diagnostics.

2.3.2. CloudSat Cloud Water Profiles and the Boreal Summer MJO

The CloudSat cloud radar provides altogether new information on cloud hydrometeors, specifically vertically-resolved ice and liquid water contents (IWC, LWC) (Stephens et al. 2002). Such data provides constraints on model fields that have simply never been available but yet are key to constraining and validating key cloud/convective processes. However, considerations of this as a model diagnostic requires significant care due to the different representations of the ice and water fields in the model versus the observations (Waliser et al. 2009). As a consideration of this as a model diagnostic, Jiang et al. (2010), use these new observations to examine the cloud vertical structure of the boreal summer MJO (referred to here as the boreal summer intraseasonal oscillation; BSISO). Fig. 9a-d illustrates the vertical-meridional structures of LWC and IWC associated with the northward propagation of the BSISO. Both LWC and IWC composites are based on CloudSat estimates and ERA-Int reanalysis. Both are analyzed by using composite analysis (very similar to the Method 1 described in Section 2.c.i) based on 10 strong northward propagating ISO events over the Indian Ocean during 2006-2008 summers (not shown). The x-axis in each panel of Fig. 9 is the relative distance to the convection center (denoted by '0'), with positive (negative) values representing north (south) to the convection center with unit of degree. Similar composite analysis for the meridional profiles of TRMM rainfall is also shown in the two lower panels (Fig.9e-f). Clearly evident is the pronounced northward shift of the enhanced LWC in the PBL relative to the convection center by about 3-4 degrees based on both CloudSat (Fig. 9a) and ERA-Int (Fig. 9c). A very similar feature in the anomalous moisture fields associated with the northward propagating BSISO has also been reported in previous studies (e.g., Jiang et al. 2004; Fu et al. 2006), which could be indicative of a pre-conditioning process for the northward propagation of the BSISO convection. The maximum IWC anomalies are observed aloft the convection center near 400hPa in both CloudSat (Fig. 9b) and ERA-Int analysis (Fig. 9d), largely in phase with (or slightly lags) ISO convection center.

While general agreement between CloudSat and ERA-Interim are found, notable differences exist as well. For example, CloudSat IWC bears much larger amplitude than that based on ERA-Interim reanalysis. This is likely due to the fact that CloudSat tends to be sensitive and thus observe all the hydrometeors (e.g., snow, cloud ice) while ERA-Interim only represents the cloud ice. This issue has been discussed in the sections below and is also discussed and illustrated in detail in Waliser et al (2009). Meanwhile, stronger magnitude in the ERA-Interim LWC is also noted. Moreover, the maximum LWC anomalies based on CloudSat are found to the north of the convection center in the

PBL. In contrast, the maximum LWC appears in the mid-troposphere above the convection center based on the ERA-Interim. This latter difference may arise due to biases in the LWC retrieval in the context of overlying clouds and precipitation. Further analysis based on CloudSat data indicates that IWC variability of the BSISO is largely associated with deep convective clouds, while LWC is mainly linked to alto-cumulus at mid-level and stratus/stratocumulus cloud at low-level (not shown).

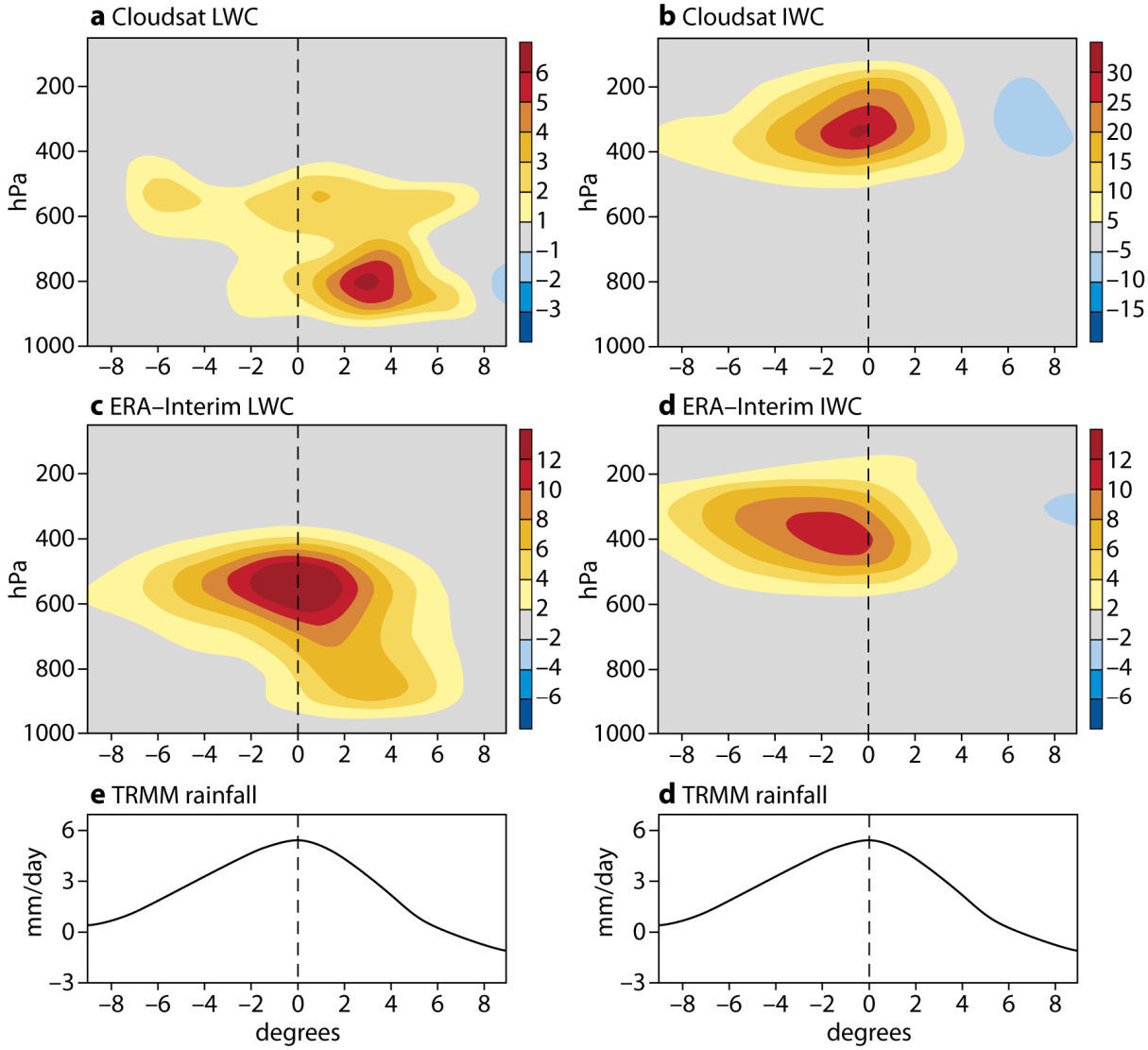

Figure 9. Composite meridional-vertical structures of LWC (left panels), IWC (right panels) based on CloudSat (upper panels) and ERA-Int reanalysis (lower panels). Meridional profile of the composite rainfall is also displayed in lower two panels. X-axis in each panel is the meridional distance (deg) with respect to the BSISV convection center. The positive (negative) value means to the north (south). All variables are averaged over 70-95°E. Note that the color scales are different in panels a-d. Adopted from Jiang et al. (2010).

2.3.3. TRMM Diabatic Heating Profiles and the MJO

To try and better understand propagation and maintenance mechanisms of the MJO, relate these to theory, and constrain model physical parameterizations – particularly of deep convection and stratiform cloud processes, information on the vertical structure of diabatic heating is sorely needed. Fortunately, within the last few years, a number of products based on TRMM have been developed that attempt to retrieve the vertical structure of latent heating. Here we illustrate some results from Jiang et al. (2009) who utilized recently updated heating estimates based on the Tropical Rainfall Measuring Mission (TRMM) from two different latent heating and rainfall retrievals and one radiative heating estimate based on a combination of satellite measurements and model radiation calculations. Heating structures from two different versions of the European Centre for Medium-Range Weather Forecasts (ECMWF) reanalyses/forecasts are also examined. Due to the limited period of available datasets at the time of this study, they focus on the winter season from October 1998 to March 1999.

Figure 10 illustrates the time evolution of vertical Q_1 structures of the 'Trained' Radiometer Heating (hereafter TRMM-TRAIN; Grecu and Olson 2006; Grecu et al. 2009; Fig. 10d) and the Convective-Stratiform Heating (TRMM-CSH; Tao et al. 1993, 2000, 2001; Fig. 10e) algorithms, as well as the ECMWF Integrated Forecast System (EC-IFS; Fig. 10a) and ERA-40 reanalyses (Fig. 10b). The time evolution of corresponding rainfall fields is also displayed in two lower panels. All above fields are calculated over the eastern equatorial Indian Ocean (75-95^{o}E; 10^{o}S-10^{o}N) during the period from October 1998 to March 1999, with their corresponding seasonal mean during this period removed to highlight their variability components.

The modulation of rainfall associated with the MJO is readily discerned in both TRMM 3B42 rainfall estimates and ERA-40 reanalysis (Fig. 10c). The two other TRMM heating/rainfall estimates display similar features as exhibited by the TRMM 3B42 product (Fig. 10f). Consistent with the rainfall evolution, the vertical heating structures also display strong subseasonal variations associated with the MJO events in all four datasets. Although seasonal mean heating structure in the two ECMWF datasets exhibits much stronger amplitude than that in the TRMM estimates (not shown), anomalous heating structures based on various datasets exhibit greater similarity to each other including the amplitudes and vertical structures, although slight difference in the position of vertical heating maxima can still be discerned. Comparable amplitudes and evolution of the anomalous rainfall evolution from these datasets in the lower two panels in Fig. 10 are also consistent with the anomalous vertical heating structures.

When interpreting the differences in the heating and rainfall structures between the models (ECMWF products in this case) and the TRMM estimates, there are a number of caveats that need to be kept in mind. These are discussed in more detail in Jiang et al. (2009) but will be highlighted briefly here. First, there is a sampling issue between the two TRMM estimates. The variables $Q_1 - Q_R$ and Q_1 are generated by TRAIN and CSH algorithms respectively. In addition, both variables are only computed on grid points where surface rainfall is detected. Thus, in order to facilitate a comparison between these two TRMM estimates, and the TRMM Q_R estimates are needed to derive an equivalent Q_1 based on both TRAIN $Q_1 - Q_R$ and CSH Q_1. For future developments, standard outputs of the TRMM heating estimates based on different algorithms would be helpful to reduce biases due to these sampling issues. Second, it is also noted that the eddy sensible heat flux is not considered in either TRMM algorithm over non-precipitating region; while they are included in the ECMWF values. Thus, comparison of the heating structures between the ECMWF values and the TRMM estimates near the

surface should be considered with caution. Third, definitions of the convective and stratiform clouds are different in the ECMWF values and TRMM estimates. In the TRMM estimates, the separation of convective and stratiform precipitation mainly depends on the identification of a 'bright band' and a threshold of the reflectivity (e.g., Awaka et al. 1997). In the GCM, while convective precipitation is estimated by the sub-grid scale parameterization scheme, its stratiform counterpart is calculated by considering the condensation due to grid-scale updraft. Thus, the partitioning of convective/stratiform precipitation in the models could be sensitive to the horizontal resolution of the grid system adopted. Fourth, it is also noteworthy that while the TRMM estimates provide unprecedented benchmarks to validate the current general circulation models, the algorithms on which these estimates are based still heavily depend on high-resolution cloud-resolving models, which are subject to parameterization schemes for sub-grid processes in the model. Fifth, there is some uncertainty as to the degree the TRMM estimates are able to represent heating from shallow cumulus and precipitating stratocumulus clouds, thus another reason to be cautions about interpretations in or near the boundary layer.

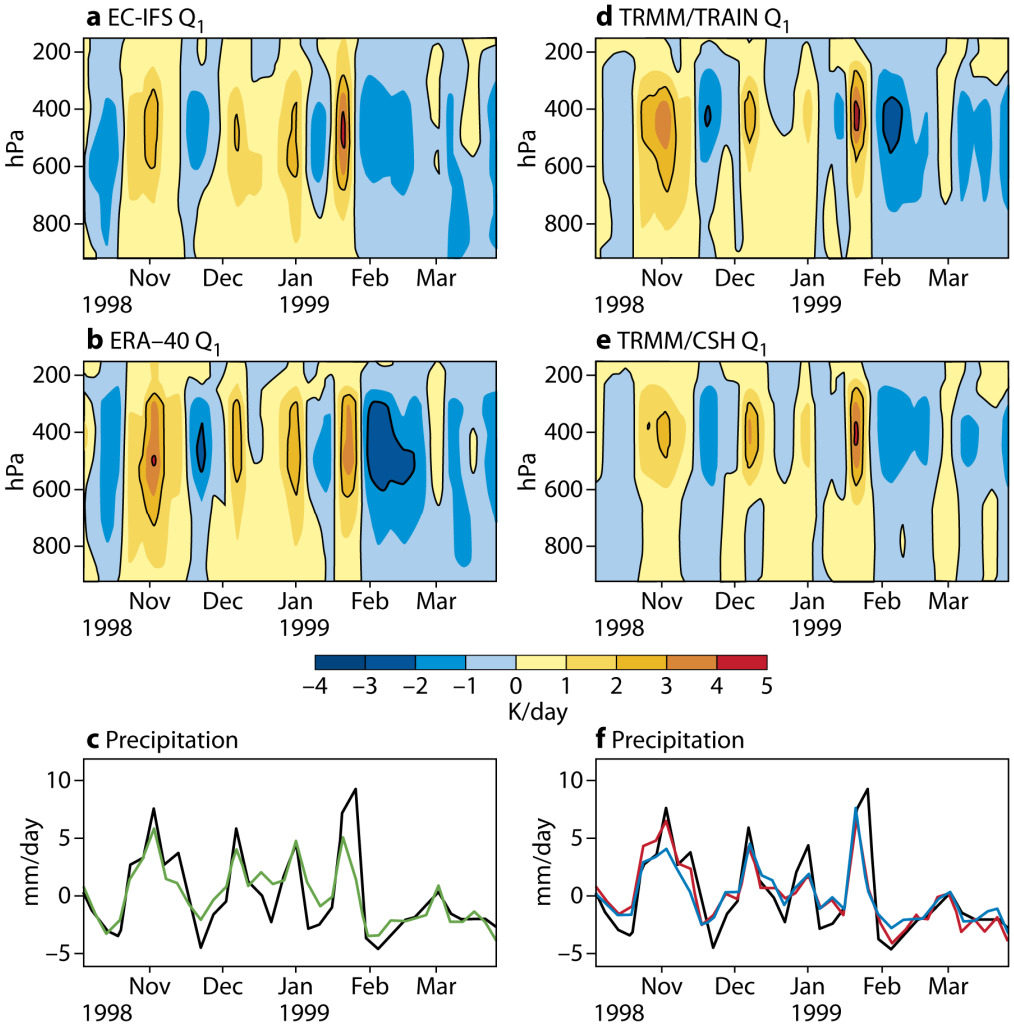

Figure 10. Time-pressure Q_1 structures (units: K day^{-1}) during the 1998/99 winter based on (a) EC-IFS forecast; (b) ERA-40 reanalysis; (d) TRMM/TRAIN; and (e) TRMM/CSH estimates. (e) and (f): Time evolution of rainfall (units: mm day^{-1}) based on various datasets: TRMM 3B42 (black), ERA-40 (green), TRMM/TRAIN (orange), TRMM/CSH (blue). TRMM 3B42 rainfall is duplicated in (e) and (f) as a reference. All heating and rainfall fields are anomalies relative to their corresponding seasonal mean values during the period of Oct. 1998 – Mar. 1999, and are averaged over the equatorial eastern Indian Ocean (75-95°E; 10°S-10°N). Adopted from Jiang et al. (2009).

2.3.4. CloudSat Ice and Liquid Water Content Profiles

In most conventional GCMs such as the European Centre for Medium-Range Weather Forecasts (ECMWF) and the NASA Goddard Earth Observing System V.5 (GEOS5), the prognostic frozen and liquid water mass are determined by parameterizations. The parameterizations typically divide the total condensates into an amount that remains suspended or floating in the modeled atmosphere (i.e., cloud ice and liquid) and an amount that falls out as precipitation (i.e., snowfall and rainfall). However, CloudSat estimates of vertically resolved IWC and LWC are sensitive to ice and liquid particles of nearly all sizes, limited by the minimum detectable power and attenuation (Austin et al. 2008). Such values may be appropriate for comparing to the total ice and liquid from a multi-species microphysical models referred to collectively in this study as Cloud-Resolving Model (CRM)-like GCMs (e.g., GSFC fvMMF; Tao et al., 2009). To help address this problem and utilize the CloudSat measurements, it is possible to make judicious subsets of the CloudSat data based on additional flags and information in the retrieval products [*Stephens et al.*, 2008].

In order to obtain cloud IWC/LWC from CloudSat that are not, for example, 'contaminated' with larger precipitating hydrometeors and thus are more appropriate for GCM validation, we follow the approaches of Li et al., [2008] for LWC and Waliser et al. [2008] for IWC. The specific subsampling/filtering employed here for LWC is designed to exclude retrievals when precipitating hydrometeors are present by using the CloudSat precipitation flag to identify retrievals associated with precipitation at the surface (NP-LWC). For IWC, the subsampling is to exclude all the retrievals in any profile flagged as precipitating at the surface (NP) and exclude the retrievals that are flagged as 'convective' (NC), where 'convective' includes the 'deep convection' and 'cumulus' cloud classification (NPC-IWC). This sampling is intended to filter out the samples/profiles that have large falling hydrometeors and thus serve as a preliminary estimate of the IWC/LWC for 'cloud-only' conditions more fitting for comparison to some conventional GCMs. For example, Figure 11 shows CloudSat IWC values filtered in three different ways, taking only cases that are flagged as having no precipitation (NP; b) at the ground, classified as non-convective (NC) clouds, and the combination of both of these criteria (NP & NC). The total IWC without any filtering is shown in Figure 11a. For interpretation of Figure 11, it is useful to start with the most stringently filtered case, i.e. NP & NC. In this case, the IWC is considerably lower than the total shown in Figure11a. Interestingly, this fraction of retained ice – inferred here to be the 'floating' cloud ice – is within a factor of 2 or so of the same fraction of cloud to total ice as in the two CRM-like GCMs shown in Figure 11 which will be described in the following. Note, if this aspect was taken into account in the analysis depicted in on the right side of Figure 11b & c, the CloudSat IWC values would be significantly reduced in magnitude and the agreement would be considerably better.

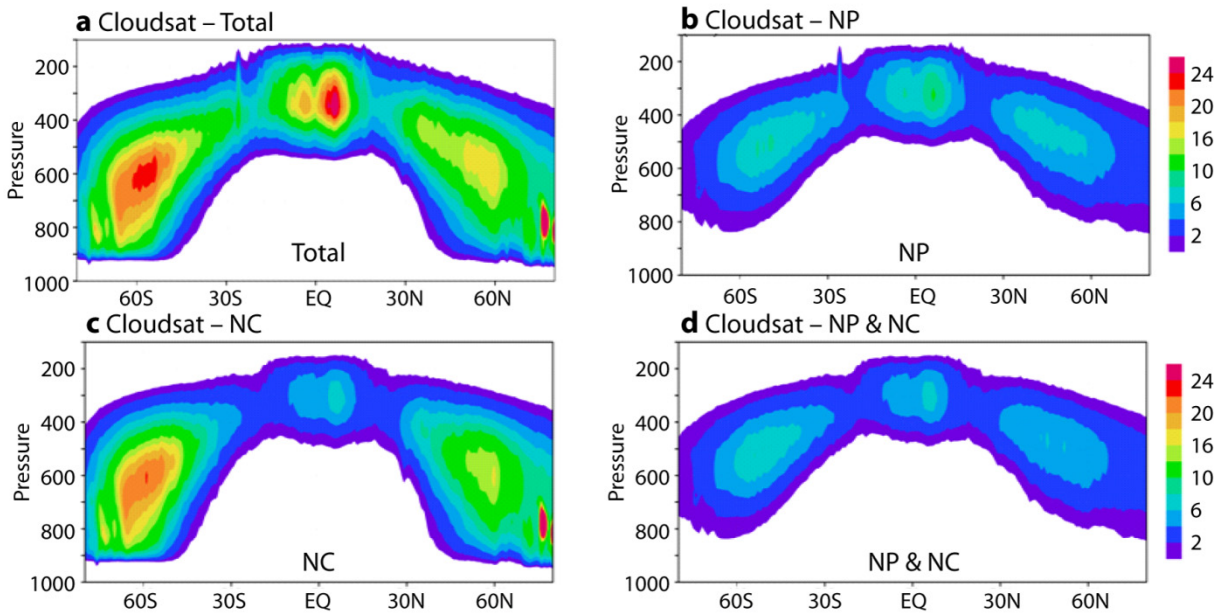

Figure 11. Annual and zonal mean values of CloudSat IWC (mg m^{-3}) for total (TOTAL;a), when considering clear cases and those with IWC > 0 but flagged as having no precipitation at the surface (NP; b), cases flagged as non-convective clouds (NC; c), and those cases that meet either of these criteria (NP or NC; d).

Unlike the conventional GCMs, some CRM-like GCMs utilize the multi-species ice framework trying to more explicitly account for the representation of sub-grid scale processes. In what is now commonly referred to as the multi-scale modeling framework (MMF; also known as 'Super parameterization'), the conventional cloud parameterizations are replaced with a CRM in each host GCM grid column [*Grabowski*, 2001; *Khairoutdinov and Randall*, 2001; *Randall et al.*, 2003]. While this aspect deserves mention, the most relevant point of the discussion is that their ice microphysical schemes include representations of cloud ice, snow and graupel, which allow for an additional consideration in terms of the model-data comparisons. In here, two CRM-like GCMs are used. The NASA fvMMF was developed using a finite volume GCM (fvGCM) with 2^{o}x2.5^{o} resolution and a version of the two-dimensional (2D) Goddard Cumulus Ensemble (GCE) model [*Tao et al.*, 2003] embedded in each GCM grid box. The fvMMF employs a single-moment bulk microphysical scheme with two liquid (cloud and rain) and three frozen (cloud, snow and graupel) hydrometeor classes. Kuang et al. [2005], on the other hand, proposed a different kind of approach for improving the cumulus scale called Diabatic Acceleration and REscaling or Reduced Acceleration in the VErtical (DARE/RAVE). DARE/RAVE is a computationally efficient method for simulating the interactions of large-scale atmospheric circulations with deep convection in a 3D cloud-resolving model by reducing the scale difference between the large-scale and convective circulations. The microphysics scheme used in this model is a single-moment, 6-class microphysics scheme that includes the interaction between water vapor, cloud water, cloud ice, rain, snow, and graupel [*Hong and Lim*, 2006].

Figure12 shows the zonal and annual mean vertical profiles of IWC from the two CRM- GCMs. Except for the distributions of cloud ice, the distributions for the other frozen components from the two models agree relatively well, particularly given the complete lack of global observations that would adequately guide and constrain GCM development in this area. Notable is the relatively good agreement in the total IWC values in this figure, namely in terms of general morphology and

magnitude, with those of CloudSat shown in Figure 11a. For CloudSat, the greatest concentration of IWC is between 250 and 400 hPa, while for the models the peak values are found around 500-600 hPa. Presuming such distributions relate in some way to the latent and radiative heating profiles, this disagreement is somewhat troubling and might indicate shortcomings in the underlying microphysical schemes in these models as they relate to convection and the large-scale circulation. Consideration should also be given to the possibility that the height of the peak CloudSat values might also be artificially influenced by the algorithm's method of (linearly) combining the liquid and ice water retrieval solutions via temperature.

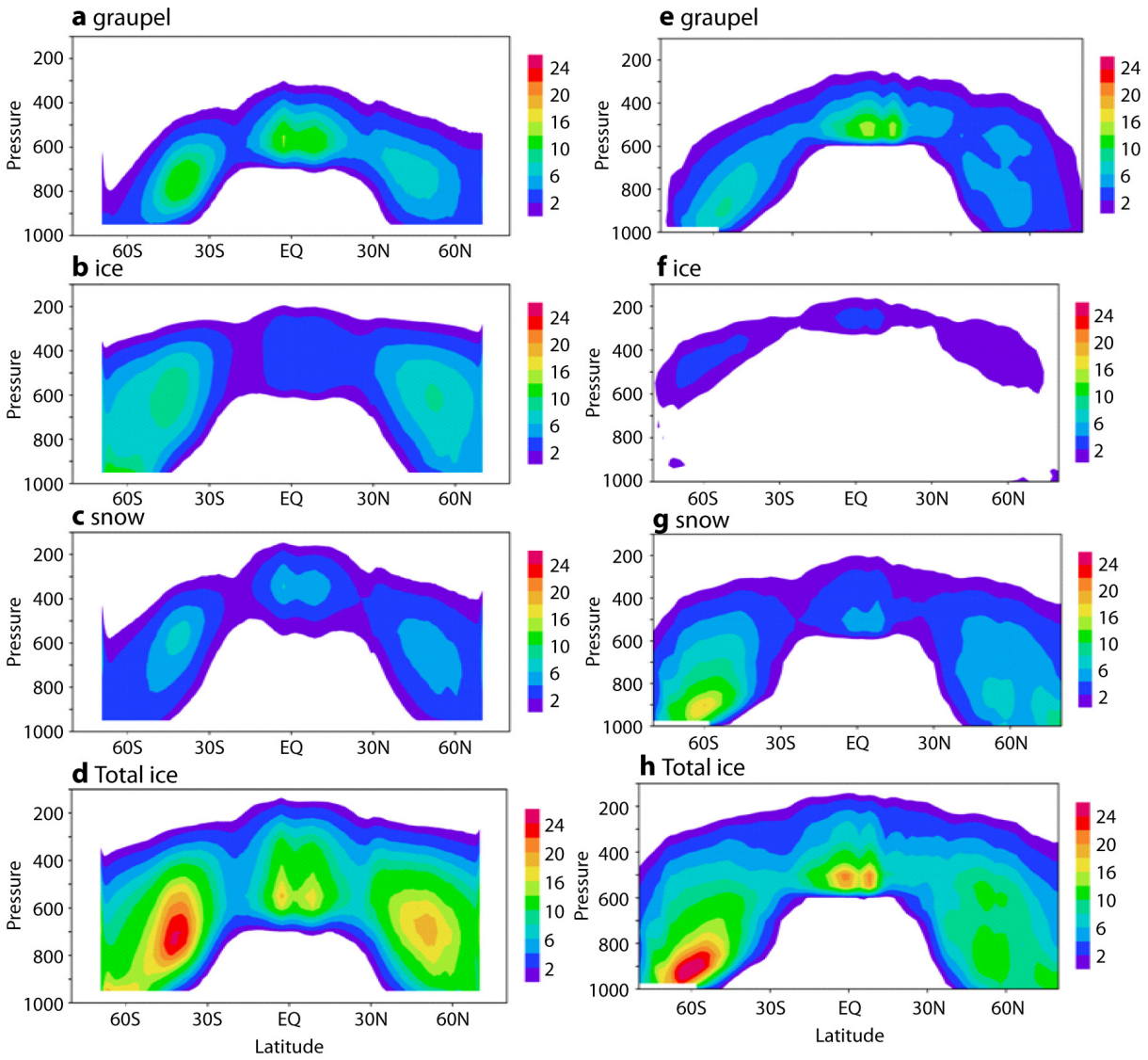

Figure 12. Annual and zonal mean values of IWC (mg m^{-3}) for (a and e) graupel, (b and f) cloud ice, (c and g) snow, and (d and h) their sum from the (left) RAVE and (right) NASA fvMMF GCM.

As an additional consideration, we illustrate a set of comparisons between the CloudSat values of IWC and LWC and a number of modeled values along the GEWEX Pacific Cross-section (GEWEX Pacific Cross-section Intercomparison: GPCI; Teixeira et al. 2010). In this case, the cross-section transects the entire transition from boundary layer (BL) stratocumulus (Sc), trade-wind cumulus to deep cumulus cloud types, acts as a component of the diagnostic/metric itself; and in fact is the main objective of the GPCI design. In this case, CloudSat, ECMWF analyses, and two models are evaluated in terms of their ability to represent the vertical cloud structures along the transect focusing on their ability to represent the three fundamental cloud regimes mentioned above.

Figure 13a shows seasonal mean (JJA-2006) vertical profiles along the cross section from CloudSat for *total* LWC (13a1), total IWC (13a2), total LWC+IWC (13a3). For nearly all regions, CloudSat (Fig. 13a) indicates that the greatest concentration of LWC is below 750 hPa over the subtropical regions and extends up to about 400 hPa in the deep Tropics with relatively high mass concentrations of IWC at upper levels. The resulting LWC conditionally sampled as described above for NP-LWC (Fig. 13b1), the NPC-IWC (Fig. 13b2), and the sum of NP-LWC & NPC-IWC (Fig. 13b3). Shown in Figure 13a1 & 13b1, it is clear that the CloudSat LWC associated with conditions where precipitation is detected at the surface is a substantial component of the CloudSat LWC in the cross section. Note that the cloud base/cloud top of the NP-LWC subsample tends to be lower/higher than the total LWC.

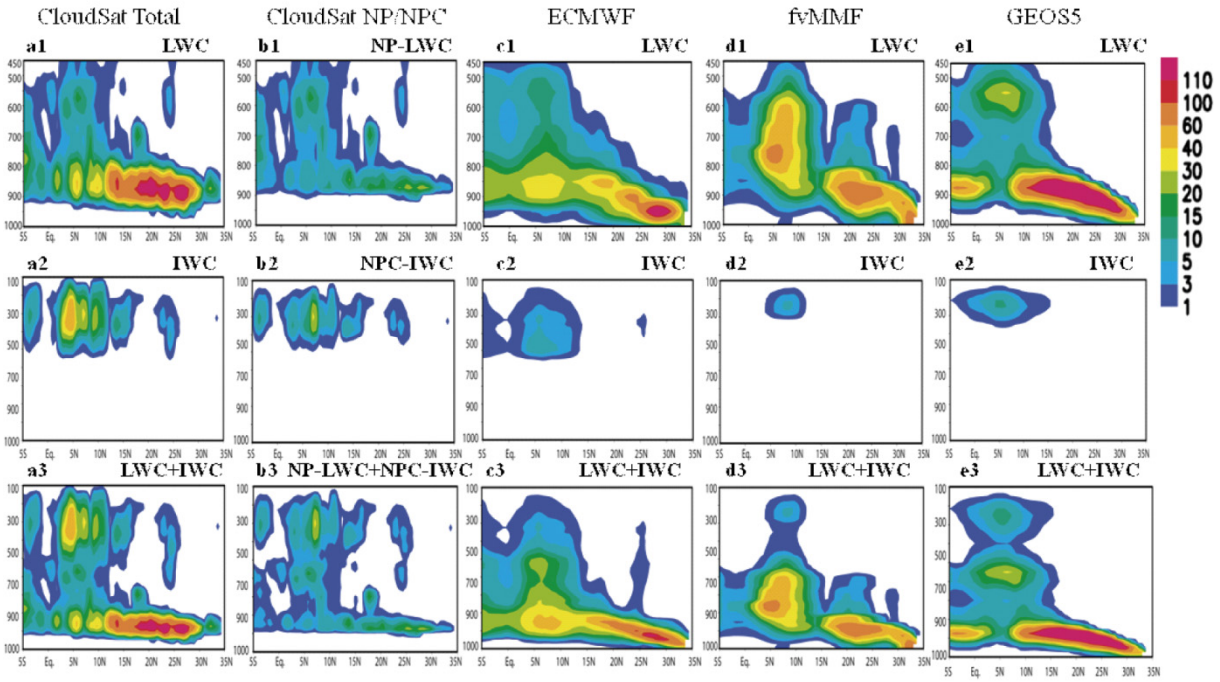

Figure 13. The cross section monthly (JJA-2006) average values of cloud liquid water content (upper row - a; pressure scale: 1000-450 hPa,LWC; mg m-3), cloud ice water content (middle row - b; IWC; mg m-3), and total cloud mass (low row – c; mg m-3), from (a1) CloudSat for total LWC, (a2) CloudSat for total IWC and (a3) CloudSat for total LWC+IWC; The same but for (b1) CloudSat non-precipitating NP-LWC, (b2) CloudSat non-precipitating & non-convective NPC-IWC and (b3) CloudSat NPC-IWC+NP-LWC. The same but for ECMWF R31 (c1 ~ c3) for ECMWF R31 analysis. Note that the color scale is different from other figures for IWC. The same but for fvMMF (d1 ~ d3). The same but for GEOS5 GCM (e1 ~ e3).

IWC and LWC values from ECMWF analysis and output from GEOS5 and fvMMF GCMs are also illustrated in Figure 13. All model and analyses output are based on specifying sea surface temperatures (SSTs) from June to August 2006. All the models have been converted from cloud water/ice mixing ratio (kg kg^{-1}) to LWC/IWC (mg m^{-3}) using model temperatures and pressures and re-gridded to a common 2°x 2° latitude-longitude grid. Note that the ECMWF LWC/IWC values are from the CY30r1 version of the IFS system that includes the upgraded treatment of Sc (Köhler, 2005). Figure 13 (c1 - c3) shows the seasonal mean (JJA-2006) vertical profiles from the ECMWF analysis for LWC (13c1), IWC (13c2) and LWC+IWC (13c3). Although agreeing in a qualitative manner, the morphology of the IWC/LWC varies considerably between the CloudSat retrievals and the analysis values. The depth of the vertical extent of LWC from ECMWF (Fig. 13c1) clearly increases from colder towards warmer SSTs along the trades, while the CloudSat exhibits slightly less increase (Fig. 13a1). In the region north of 15 N^o, the ECMWF cloud base is lower than CloudSat. The peak LWC values in ECMWF are the highest near 30 N (at about 950 hPa) while CloudSat's is around 20-25N (above 900 hPa). In the Tropics near the ITCZ, the ECMWF analysis exhibits slightly larger LWC values with more LWC extending above 750 hPa than estimated by CloudSat. The ECMWF (2c1) IWC values are typically lower than CloudSat total IWC (13a1) by a factor of 2~3.

Figure 13 also shows the cross sections of mean values of LWC/IWC from fvMMF (13d1/13d2) and GEOS5 (13e1/2e2) - in both cases the values only represent the mass in CloudSat not including any precipitating components. In the subtropics, similar to that in ECMWF, the LWC distribution from both models shows a cloudy BL capped by a cloud-free atmosphere above. The models' cloud bases north of 15 N^o are clearly lower than CloudSat's. The inversion height increases from the Sc regions to the deep tropics. In tropical regions, the CloudSat LWC at mid tropospheric levels is more confined and has smaller values than any of the model vertical distributions. This probably due to the IWC/LWC retrieval is performed artificially with a constraint based on ECMWF analyses temperature; the composite profile is obtained by using the LWC retrieval for bins warmer than 0°C, the IWC retrieval for bins colder than -20°C, and a linear combination of the two in the intermediatetemperature range. The vertical distribution of LWC from fvMMF exhibits much larger LWC values in the deep Tropics, when compared with the satellite values or the analysis, extending up to and above 500 hPa. It makes sense that a model like fvMMF would have much more LWC above freezing level due to lifting by cloud circulations resolved by the CRMs embedded in the fvMMF model grid. On the other hand, CloudSat IWC values are artificially limited in these regions by the algorithm. Figure 13 (d2&e2) show that the IWC simulated by both GEOS5 and fvMMF are about half as large as the CloudSat values with the peak values being located at similar altitudes.

The LWC from ECMWF (Fig. 13c1) is in general larger than the NP-LWC CloudSat estimates (Fig. 2b1). In the subtropical BL, when compared to subsampled CloudSat NP-LWC, both fvMMF and GEOS5 produce larger amounts of LWC when compared with CloudSat NP-LWC. The fvMMF shows a cloud structure between 20 and 25 N that is deeper than the typical BL depth and does not appear in the other datasets. As shown in Figure 13a2 & 13b2, the removal of the larger IWC values reduces the NPC-IWC values (Fig. 13b2) by a factor of 2. The ECMWF (13c2), fvMMF (12d2) and GEOS5 (13e2) IWC values compare favorably to the CloudSat NPC-IWC, with the peak values being located at similar altitudes.

3. Summary

The objective of this presentation was to illustrate a number of efforts to develop diagnostics for key processes and phenomena in the Tropics. This included formal diagnostics developed for the MJO by the CLIVAR MJO Working Group. The motivation for their development was the significant interest in improving climate and weather prediction models in regards to their simulations of the MJO. These diagnostics, while well-motivated, well formulated, well documented and relatively easy to apply to a model setting, are primarily of use in helping to evaluate a given GCM's performance. However, due to their more traditional nature and traditional data sources, they do not provide much insight into why a model may be particularly good or bad. Very few if any are process oriented and of those that might be insightful by looking at vertical structure still necessarily relied on analyses values which of course have a strong model component to them. As an aside, the newly formed WCRP-WWRP/THORPEX MJO Task Force (www.ucar.edu/yotc/mjo.html) is specifically charged to develop more process-oriented diagnostics and metrics to help provide more insight into model shortcomings and strengths and guide their improvements.

In exploring additional options for providing more insightful, physically probing and/or observation-based diagnostics for the MJO, we have explored and illustrated the use of a number of satellite products. This included AIRS profiles of temperature and water vapor,, CloudSat profiles of IWC and LWC, and TRMM-based profiles of latent heating. In the case of AIRS profiles of temperature and water vapor, their use as an MJO diagnostic was demonstrated to be quite robust relative to data record length and sampling/compositing methodology. CloudSat profiles of IWC and LWC represent altogether new resources for model evaluation and for particularly difficult fields. However, a number of important considerations need to be taken when making model data comparisons of these data to modeled quantities – in particular considerations of what aspects of the hydrometeor field (e.g., snow, rain, cloud ice, cloud water, graupel) are being modeled versus measured. Recently developed TRMM profiles of latent heating represent a near holy grail of model verification for the Tropics but they too come with significant caveats, not the least of which is that they have some model-based elements, have sensitivity issues in/near the boundary layer, and have some nuances in terms of representations of the radiation and eddy flux fields as well as their treatments of convective versus stratiform rainfall.

We recommend that such satellite products as well as their blended counterparts, which in some cases might be analyses or combined model-observation retrieval products continue to be explored and applied to model evaluations. In some cases, the mismatches between model and data variable representation might be alleviated if the models and observations were more commonly brought together and the challenges (and potential opportunities) relayed to the observation and modeling teams. Moreover, we recommend that programmatic activities such as the MJO Task Force and GCSS GPCI be promoted and engaged in. As new satellite missions are designed and developed, it is paramount for the interactions between the mission designers and modeling groups to be established as early as possible in order that the most utility can be gained from the new measurements.

Acknowledgements

This research was carried out at Jet Propulsion Laboratory, California Institute of Technology under a contract with National Aeronautics and Space Administration. BT acknowledges partial support from ATM-0840755, a grant from the National Science Foundation to University of California, Los Angeles. XJ acknowledges support from NSF under Award ATM-0934285 and NOAA under Award NA09OAR4310191.

4. References

Agudelo, P. A., J. A. Curry, C. D. Hoyos, and P. J. Webster, 2006: Transition between suppressed and active phases of intraseasonal oscillations in the Indo-Pacific warm pool. J. Climate, 19, 5519-5530.

Awaka, J., T. Iguchi, H. Kumagai, and K. Okamoto (1997), Rain type classification algorithm for TRMM precipitation radar, paper presented at Geoscience and Remote Sensing, 1997. IGARSS '97. Remote Sensing - A Scientific Vision for Sustainable Development., 1997 IEEE International.

Austin, R. T., A. J. Heymsfield, and G. L. Stephens (2009), Retrieval of ice cloud microphysical parameters using the CloudSat millimeter-wave radar and temperature, J. Geophys. Res., doi:10.1029/2008JD010049.

Chahine, M. T., and Coauthors, 2006: AIRS: Improving weather forecasting and providing new data on greenhouse gases. Bull. Amer. Meteor. Soc., 87, 911-926, doi:10.1175/BAMS-87-7-911.

CLIVAR MJO Working Group, 2009: MJO simulation diagnostics. J. Climate, 22, 3006-3030, 10.1175/2008jcli2731.1.

Fu, X. H., B. Wang, and L. Tao, 2006: Satellite data reveal the 3-D moisture structure of tropical intraseasonal oscillation and its coupling with underlying ocean. Geophys. Res. Lett., 33, L03705, doi:10.1029/2005GL025074.

Grabowski, W. W. (2001), Coupling cloud processes with the large-scale dynamics using the Cloud-Resolving Convection Parameterization (CRCP), J. Atmos. Sci., 58(9), 978 – 997, doi:10.1175/1520-0469(2001)058 <0978:CCPWTL>2.0.CO;2.

Grecu, M. and W. S. Olson, 2006: Bayesian estimation of precipitation from satellite passive microwave observations using combined radar-radiometer retrievals. Journal of Applied Meteorology and Climatology, 45, 416-433.

Grecu, M., W. S. Olson, C. L. Shie, T. S. L'Ecuyer, and W. K. Tao (2009), Combining Satellite Microwave Radiometer and Radar Observations to Estimate Atmospheric Heating Profiles, J. Climate, 22(23), 6356-6376.

Gualdi, S., et al. (1999), The interannual variability of the Madden-Julian Oscillation in an ensemble of GCM simulations, Climate Dynamics, 15(9), 643-658.

Hendon, H. H. (2000), Impact of air-sea coupling on the Madden-julian oscillation in a general circulation model, Journal of the Atmospheric Sciences, 57(24), 3939-3952.

Hendon, H. H., et al. (1999), Interannual variation of the Madden-Julian oscillation during austral summer, Journal of Climate, 12(8), 2538-2550.

Hendon, H. H., et al. (2007), Seasonal dependence of the MJO-ENSO relationship, Journal of Climate, 20(3), 531-543.

Hong, S.-Y., and J.-O. J. Lim (2006), The WRF Single-Moment 6-Class Microphysics Scheme (WSM6), J. Korean Meteorol. Soc., 42, 129– 151.

Huffman, G. J., and Coauthors, 2007: The TRMM multisatellite precipitation analysis (TMPA): Quasi-global, multiyear, combined-sensor precipitation estimates at fine scales. J. Hydrometeorol., 8, 38-55, 10.1175/jhm560.1.

Inness, P. M., et al. (2003), Simulation of the Madden-Julian oscillation in a coupled general circulation model. Part II: The role of the basic state, Journal of Climate, 16(3), 365-382.

Jiang, X., D. E. Waliser, J.-L Li, and C. Woods, 2010: Vertical structures of cloud water associated with the boreal summer intraseasonal oscillation based on CloudSat observations and ERA-Interim reanalysis. Climate Dynamics, submitted.

Jiang, X., Duane E. Waliser, William S. Olson, Wei-Kuo Tao, Tristan S. L'Ecuyer, Jui-Lin Li, Baijun Tian, Yuk L. Yung, Adrian M. Tompkins, Stephen E. Lang, and Mircea Grecu, 2009: Vertical heating structures associated with the MJO as characterized by TRMM estimates, ECMWF Reanalyses and forecasts: A case study during 1998-99 winter. J. Climate, 22, 6001-6020.

Jiang, X., T. Li, and B. Wang (2004) Structures and Mechanisms of the Northward Propagating Boreal Summer Intraseasonal Oscillation. J. Clim. 17:1022-1039.

Kang, I. S., et al. (2002), Intercomparison of the climatological variations of Asian summer monsoon precipitation simulated by 10 GCMs, Climate Dynamics, 19, 383-395.

Kessler, W. S. (2001), EOF representations of the Madden-Julian oscillation and its connection with ENSO, Journal of Climate, 14(13), 3055-3061.

Khairoutdinov, M. F., and D. A. Randall (2001), A cloud resolving model as a cloud parameterization in the NCAR Community Climate System Model: Preliminary results, Geophys. Res. Lett., 28(18), 3617 – 3620, doi:10.1029/2001GL013552.

Kikuchi, K., and Y. N. Takayabu, 2004: The development of organized convection associated with the MJO during TOGA COARE IOP: Trimodal characteristics. Geophys. Res. Lett., 31, L10101, doi:10.1029/2004GL019601.

Kim, D., K. Sperber, W. Stern, D. Waliser, I.-S. Kang, E. Maloney, S. Schubert, W. Wang, K. Weickmann, J. Benedict, M. Khairoutdinov, M.-I. Lee, R. Neale, M. Suarez, K. Thayer-Calder, and G. Zhang. 2010: Application of MJO Simulation Diagnostics to Climate Models, J. Climate, 22(23), 6413-6436.

Köhler, M., 2005. Improved prediction of boundary layer clouds. ECMWF Newsletter 104: 18-22.

Kuang, Z., P. N. Blossey, and C. S. Bretherton (2005), A new approach for 3D cloud-resolving simulations of large-scale atmospheric circulation, Geophys. Res. Lett., 32, L02809, doi:10.1029/2004GL021024.

Lau, W. K. M. (2005), ENSO Connections, in Intraseasonal Variability of the Atmosphere-Ocean Climate System, edited by W. K. M. Lau and D. E. Waliser, Springer, Heidelberg, Germany.

Lau, W. K. M., and D. E. Waliser (Eds.) (2005), Intraseasonal Variability of the Atmosphere-Ocean Climate System, 474 pp., Springer, Heidelberg, Germany.

Lau, W. K. M., and D. E. Waliser, Eds., 2005: Intraseasonal Variability of the Atmosphere-Ocean Climate System. Springer, 474 pp.

Li, J.-L. F. and co-authors (2008), Comparisons of satellites liquid water estimates to ECMWF and GMAO analyses, 20th century IPCC AR4 climate simulations, and GCM simulations, Geophys. Res. Lett., 35, L19710, doi:10.1029/2008GL035427.

Lin, J. L., and Coauthors, 2006: Tropical intraseasonal variability in 14 IPCC AR4 climate models. Part I: Convective signals. J. Climate, 19, 2665-2690.

Madden, R. A., and P. R. Julian (1971), Detection of a 40-50 day oscillation in the zonal wind in the tropical Pacific, J. Atmos. Sci., 28, 702-708.

Madden, R. A., and P. R. Julian (1972), Description Of Global-Scale Circulation Cells In Tropics With A 40-50 Day Period, J. Atmos. Sci., 29(6), 1109-1123.

Randall, D., M. Khairoutdinov, A. Arakawa, and W. Grabowski (2003), Breaking the cloud parameterization deadlock, Bull. Am. Meteorol. Soc., 84(11), 1547– 1564, doi:10.1175/BAMS-84-11-1547.

Salby, M. L., and H. H. Hendon (1994), Intraseasonal Behavior of Clouds, Temperature, and Motion in the Tropics, Journal of the Atmospheric Sciences, 51(15), 2207-2224.

Slingo, J. M., et al. (1996), Intraseasonal oscillations in 15 atmospheric general circulation models: Results from an AMIP diagnostic subproject, Climate Dynamics, 12(5), 325-357.

Slingo, J. M., P. M. Inness, and K. R. Sperber, 2005: Modeling. Intraseasonal Variability of the Atmosphere-Ocean Climate System, W. K. M. Lau, and D. E. Waliser, Eds., Springer, 361-388.

Sperber, K. R., et al. (2005), The Madden-Julian oscillation in ECHAM4 coupled and uncoupled general circulation models, Climate Dynamics, 25(2-3), 117-140.

Stephens, G. L., and others (2002), The cloudsat mission and the a-train - A new dimension of space-based observations of clouds and precipitation, Bull. Amer. Meteor. Soc., 83(12), 1771-1790.

Stephens, G. L., and co-authors, (2008), The CloudSat mission: Performance and early science after the first year of operation, J. Geophys. Res.,doi:10.1029/2008JD009982.

Tao, W. K., et al., 2000: Vertical profiles of latent heat release and their retrieval for TOGA COARE convective systems using a cloud resolving model, SSM/I, and ship-borne radar data. J. Meteorol. Soc. Japan, 78, 333-355.

Tao, W. K., S. Lang, J. Simpson, and R. Adler, 1993: Retrieval Algorithms for Estimating the Vertical Profiles of Latent-Heat Release - Their Applications for TRMM. J. Meteorol. Soc. Japan, 71, 685-700.

——, 2001: Retrieved vertical profiles of latent heat release using TRMM rainfall products for February 1988. J. Appl. Meteorol., 40, 957-982.

Tao, W. K., and others (2009), A Multiscale Modeling System Developments, Applications, and Critical Issues, Bull. Amer. Meteor. Soc., 90(4), 515-534.

Tian, B., D. E. Waliser, E. J. Fetzer, B. H. Lambrigtsen, Y. L. Yung, and B. Wang, 2006: Vertical moist thermodynamic structure and spatial-temporal evolution of the MJO in AIRS observations. J. Atmos. Sci., 63, 2462-2485, 10.1175/JAS3782.1.

Waliser, D. E., 2006: Intraseasonal variability. The Asian Monsoon, B. Wang, Ed., Springer/Praxis Publishing, 203-257.

Waliser, D. E., et al. (2003), AGCM simulations of intraseasonal variability associated with the Asian summer monsoon, Climate Dynamics, 21(5-6), 423-446.

Waliser, D. E., K. M. Lau, W. Stern, and C. Jones, 2003: Potential predictability of the Madden-Julian oscillation. Bull. Amer. Meteor. Soc., 84, 33-50.

Waliser, D., and Coauthors, 2009: MJO simulation diagnostics. J. Climate, 22, 3006-3030, 10.1175/2008jcli2731.1.

Waliser, D., and others (2009), Cloud ice: A climate model challenge with signs and expectations of progress J. Geophys. Res., 114(D00A21).

Waliser, D., et al. (2001), Interannual Sea Surface Temperature Variability and the Predictability of Tropical Intraseasonal Variability., Journal of the Atmospheric Sciences, 58, 2595-2614.

Wang, B., 2005: Theory. Intraseasonal Variability of the Atmosphere-Ocean Climate System, W. K. M. Lau, and D. E. Waliser, Eds., Springer, 307-360.

Wheeler, M. C., and H. H. Hendon (2004), An all-season real-time multivariate MJO index: Development of an index for monitoring and prediction, Monthly Weather Review, 132(8), 1917-1932.

Wheeler, M. C., and H. H. Hendon, 2004: An all-season real-time multivariate MJO index: Development of an index for monitoring and prediction. Mon. Wea. Rev., 132, 1917-1932.

Yang, B., X. H. Fu, and B. Wang, 2008: Atmosphere-ocean conditions jointly guide convection of the boreal summer intraseasonal oscillation: Satellite observations. J. Geophys. Res., 113, D11105, 10.1029/2007jd009276.

Yang, G. Y., and J. Slingo (2001), The diurnal cycle in the Tropics, Monthly Weather Review, 129(4), 784-801.

Zhang, C. D., 2005: Madden-Julian Oscillation. Rev. Geophys., 43, RG2003, doi:10.1029/2004RG000158.

Zhang, C. D., and Coauthors, 2006: Simulations of the Madden-Julian Oscillation in four pairs of coupled and uncoupled global models. Climate Dyn., 27, 573-592, 10.1007/s00382-006-0148-2.